Available online at www.sciencedirect.com
SCIENCE DIRECT®
International Journal of Heat and Mass Transfer 47 (2004) 2139–2148
International Journal of HEAT and MASS TRANSFER
www.elsevier.com/locate/ijhmt

# Optimal distribution of discrete heat sources on a plate with laminar forced convection

A.K. da Silva [a], S. Lorente [b], A. Bejan [a,*]

[a] Department of Mechanical Engineering and Materials Science, Duke University, Box 90300, Durham, NC 27708-0300, USA
[b] Department of Civil Engineering, National Institute of Applied Sciences (INSA), 135 Avenue de Rangueil, Toulouse 31077, France

Received 19 September 2003; received in revised form 1 December 2003

**Abstract**

In this paper constructal theory is applied to the fundamental problem of how to arrange discrete heat sources on a wall cooled by forced convection. The global objective is to maximize the conductance between the discrete heated wall and the fluid. This is equivalent to minimizing the temperature of the hot spot on the wall, when the heat generation rate is specified. The mechanism by which the global objective is achieved is the generation of flow configuration, in this case the distribution of discrete heat sources. Two different analytical approaches are used: (i) large number of small heat sources, and (ii) small number of heat sources with finite length, which are mounted on a flat wall. Both analyses show that the heat sources should be placed nonuniformly on the wall, with the smallest distance between them near the tip of the boundary layer. If the Reynolds number is high enough, then the heat sources should be mounted flush against each near the entrance to the channel. The analytical results are validated by a numerical study of discrete heat sources that are distributed nonuniformly inside a channel formed by parallel plates.


*Keywords:* Constructal theory; Electronics cooling; Packing; Forced convection; Discrete heat sources

## 1. Introduction

Internal forced convection continues to be one of the most active areas of heat transfer research today. The reason is the strong emphasis on the miniaturization of cooling and heating configurations, the success of which depends greatly on the optimization of flow configuration. The challenge is not only to predict thermal and fluid behavior, but also to simulate a sufficient number of flow configurations so that the effect of geometry on performance is clear.

In this arena, the emergence of constructal theory and design as an unbiased (principle based) approach to optimizing flow architecture, is worth considering. No configuration is favored a priori based on intuition—all configurations compete under the specified global constraints. Many applications of this approach have been published, and the main trends are reviewed in [1]. What flows through the structure (fluid, heat, electricity, goods) is not as important as how the structure 'morphs' in order to perform best, globally, while meeting the constraints. Most relevant to the architecture optimized in this study is a series of studies in which the *density* of heat transfer has been optimized subject to volume constraints (Ref. [1], Chapter 3).

In this paper we consider the fundamental problem of optimizing the distribution of discrete heat sources on a wall with forced convection. Several papers have been published on the heat transfer performance of walls with distributed heat sources [2–11]. Some have recognized the opportunity to improve global performance by optimizing the nonuniform distribution of discrete heat sources, for example, Refs. [6,11]. In the present paper we approach this problem analytically and numerically, and show that an optimal nonuniform distribution exists,

* Corresponding author. Tel.: +1-919-660-5309; fax: +1-919-660-8963.
*E-mail address:* dalford@duke.edu (A. Bejan).

0017-9310/$ - see front matter © 2004 Elsevier Ltd. All rights reserved.
doi:10.1016/j.ijheatmasstransfer.2003.12.009

**Nomenclature**

| | |
|---|---|
| $c_P$ | specific heat at constant pressure, $J\,kg^{-1}\,K^{-1}$ |
| $C$ | global conductance, Eq. (34) |
| $C_{th}$ | theoretical global conductance, Eq. (17) |
| $D$ | vertical spacing, m |
| $D_0$ | heat source size, m |
| $g$ | gravity, $m\,s^{-2}$ |
| $k$ | thermal conductivity, $W\,m^{-1}\,K^{-1}$ |
| $L$ | length, m |
| $n$ | iteration number, Eq. (30) |
| $N$ | number of heat sources |
| $N'$ | number of heat sources per unit of length, $m^{-1}$ |
| $P$ | pressure, $N\,m^{-2}$ |
| $Pr$ | Prandtl number |
| $q'$ | heat transfer per unit length, $W\,m^{-1}$ |
| $q''$ | continuously distributed heat flux, $W\,m^{-2}$ |
| $q''_0$ | uniform heat flux over one heat source, $q'/D_0$, $W\,m^{-2}$ |
| $Q'$ | total heat transfer rate, $W\,m^{-1}$ |
| $\mathbf{R}$ | residual vector |
| $S$ | heat source spacing, m |
| $Re$ | Reynolds number, Eq. (8) |
| $T$ | temperature, K |
| $u$ | horizontal velocity component, $m\,s^{-1}$ |
| $\mathbf{u}$ | solutions vector |
| $v$ | vertical velocity component, $m\,s^{-1}$ |
| $x, y$ | Cartesian coordinates, m |
| $x_0$ | continuously heated region, m |

*Greek symbols*

| | |
|---|---|
| $\alpha$ | thermal diffusivity, $m^2\,s^{-1}$ |
| $\rho$ | density, $kg\,m^{-3}$ |
| $\nu$ | kinematic viscosity, $m^2\,s^{-1}$ |
| $\mu$ | viscosity, $kg\,s^{-1}\,m^{-1}$ |

*Subscripts*

| | |
|---|---|
| $0, 1, \ldots, N$ | heat source index |
| max | maximum when $N = 1$ |
| 2m | maximum when $N = 2$ |
| 3m | maximum when $N = 3$ |
| th | theory |

*Superscripts*

| | |
|---|---|
| $i$ | trial mesh |
| $(\sim)$ | dimensionless variables |

that it depends on flow strength ($Re$), and that when the heat sources are sparse the optimization has a sizeable effect on global performance.

## 2. Large number of small heat sources

Consider a horizontal plate of length $L$, which is in contact with a free stream of velocity $U_\infty$ and temperature $T_\infty$. The plate is heated by line heat sources of fixed strength $q'$ [W/m]. The heat sources appear as points on the plate sketched in Fig. 1. Each line heat source extends in the direction perpendicular to the figure. The flow is two-dimensional in the laminar boundary layer regime. The number of heat sources per unit of plate length is:

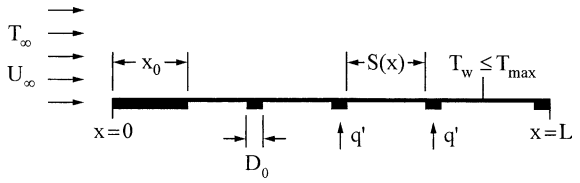


Fig. 1. The multiple length scales of the distribution of finite-size heat sources on a horizontal plate.

$$N' = \frac{\text{numbers of sources}}{\text{unit length}} \tag{1}$$

According to the constructal design, the global system (the plate and the free stream) will perform best when all its elements work as hard as the hardest working element [1]. This means that if $T_{max}$ is the maximal temperature that must not be exceeded at the hot spots that occur on the plate, then the entire plate should operate at $T_{max}$. The problem is to determine the distribution of heat sources on the plate, $N(y)$, such that the wall temperature is near the allowed limit:

$$T_w(x) = T_{max},\ \text{constant} \tag{2}$$

Assume that the density of line source is sufficiently high so that we may express the distribution of discrete $q'$ sources as a nearly continuous distribution of heat flux:

$$q''(x) = q'N' \tag{3}$$

The heat flux distribution that corresponds to Eq. (3) and $Pr \gtrsim 1$ is part of the solution for the laminar boundary layer on an isothermal wall (Ref. [12], p. 44),

$$Nu = 0.332 Pr^{1/3} Re_x^{1/2} \tag{4}$$

or

$$\frac{q''x}{k(T_{max} - T_\infty)} = 0.332 Pr^{1/3} \left(\frac{U_\infty x}{\nu}\right)^{1/2} \tag{5}$$

By eliminating $q''$ between Eqs. (3) and (5) we obtain required distribution of heat sources,

$$N'(x) = 0.332\frac{k}{q'}(T_{\max} - T_\infty)Pr^{1/3}\left(\frac{U_\infty}{\nu}\right)^{1/2}x^{-1/2} \tag{6}$$

The function $N'(x)$ represents the optimal configuration of heat sources. It shows that the sources must be positioned closer when they are near the start of the boundary layer. The total number of heat sources is

$$N = \int_0^L N'\mathrm{d}x = 0.664\frac{k}{q'}(T_{\max} - T_\infty)Pr^{1/3}Re^{1/2} \tag{7}$$

where

$$Re = \frac{U_\infty L}{\nu} \tag{8}$$

The rate of heat transfer from all the heat sources to the $T_\infty$ fluid is

$$Q'_{\max} = q'N = 0.664k(T_{\max} - T_\infty)Pr^{1/3}Re^{1/2} \tag{9}$$

This $Q'_{\max}$ expression is the same as the total heat transfer rate from an isothermal wall at $T_{\max}$. Eq. (9) represents the maximized global performance of the wall with discretely distributed heat transfer.

## 3. Heat sources with finite length

The physical implementation of the optimal distribution derived in Section 2 is limited by a manufacturing constraint: there exists a smallest scale in the design – the $D_0$ thickness of the line heat source. Features smaller than $D_0$ cannot be made. This constraint endows the design with structure, or coarseness.

The local spacing between two adjacent heat lines is $S(x)$. This spacing varies with $x$ in accordance with the optimal $N'$ distribution function, Eq. (6). Specifically, the plate length interval that corresponds to a single line heat source $q'$ is $D_0 + S(x)$. This means that the local number of heat sources per unit of wall height is

$$N'(x) = \frac{1}{D_0 + S(x)} \tag{10}$$

The strength of one source ($q'$) is spread uniformly over the finite thickness of the source ($q''_0 = q'/D_0$). The heat flux $q''_0$ is a known constant, unlike the function $q''(x)$ of Eq. (5), which is the result of design. By eliminating $N'(x)$ between Eqs. (6) and (10) we obtain the rule for how the wall heating scheme should be constructed:

$$\frac{S(x)}{L} \cong \frac{3q'Pr^{-1/3}Re^{-1/2}}{k(T_{\max} - T_\infty)}\left(\frac{x}{L}\right)^{1/2} - \frac{D_0}{L} \tag{11}$$

The spacing $S$ increases as $x$ increases. Near the start of the boundary layer, the $S(x)$ function of Eq. (11) has negative values. This means that the description provided by Eqs. (1)–(10) breaks down in a region ($0 \leqslant x \leqslant x_0$) near the start of the boundary layer. Because $D_0$ is the smallest length scale of the structure, the spacings $S$ cannot be smaller than $D_0$. We define $x_0$ as the longitudinal scale where $S$ is as small as $D_0$ in an order of magnitude sense,

$$S \sim D_0 \text{ when } x \sim x_0 \tag{12}$$

By substituting this into Eq. (11) we determine the starting length scale over which Eq. (11) is not valid

$$\left(\frac{x_0}{L}\right)^{1/2} \sim 0.664\frac{D_0}{L}\frac{k}{q'}(T_{\max} - T_0)Pr^{1/3}Re^{1/2} \tag{13}$$

In summary, the wall structure has two distinct sections. Downstream of $x \sim x_0$, the wall is heated on discrete patches of length $D_0$, which are spaced according to Eq. (11). Upstream of $x \sim x_0$, the heat sources are mounted flush against each other. We model this starting section as one with uniform heat flux, in such a way that at the end of this section (at $x \sim x_0$) the wall temperature reaches the same maximum level ($T_{\max}$) that the optimized spacings (11) are designed to maintain downstream of $x \sim x_0$. The wall temperature is $T_0$ at $x = 0$, reaches $T_{\max}$ at the transition distance $x_0$, and continues undulating at $T_{\max}$ (and slightly under) from $x_0$ until $L$.

These basic features of the optimal design are illustrated in Fig. 1. The design has multiple length scales: $L$, $D_0$, $x_0$ and $S(x)$. The first two length scales are constraints. The last two are results of global maximization of performance, subject to the constraints. Taken together, the lengths represent the constructal design—the flow architecture that brings the entire wall to the highest performance level possible.

The global heat transfer performance of the optimal design can be estimated analytically in the limit where the number of heat-source strips $D_0$ is sufficiently large. In this limit, the integral (7) applies only in the downstream region of the plate ($x_0 < x < L$), where the concentrated sources are spaced optimally according to Eq. (6). The heat transfer rate collected from $x \sim x_0$ to $x = L$ is

$$Q'_{x_0-L} \cong 0.664k(T_{\max} - T_0)Pr^{1/3}Re^{1/2}\left[1 - \left(\frac{x_0}{L}\right)^{1/2}\right] \tag{14}$$

Over the starting section of length $x_0$, we use the classical result for the wall with uniform heat flux, $Pr \gtrsim 1$ and temperature $T_{\max}$ at $x \sim x_0$, cf. Ref. [12], p. 44,

$$Q'_0 \cong 0.453k(T_{\max} - T_0)\left(\frac{U_\infty x_0}{\nu}\right)^{1/2} Pr^{1/3} \tag{15}$$

The total heat transfer rate can be expressed as

$$Q' \cong Q'_0 + Q'_{x_0-L} \cong Q'_{\max}\left[1 - 0.318\left(\frac{x_0}{L}\right)^{1/2}\right] \tag{16}$$

where the approximate character of the result stems from the order of magnitude estimation of $x_0$, Eq. (13). In the limit $x_0/L \to 0$, the total heat transfer rate $Q'$ approaches $Q'_{\max}$, because in this limit the wall temperature rises uniformly to $T_{\max}$. The right side of Eq. (13) shows that this limit is approached as $D_0/L$ decreases, and as $q'/[k(T_{\max} - T_0)]$ increases, i.e., when the heat sources are concentrated, numerous and strong.

Eq. (16) shows that the global performance of the wall heating structure can be summarized by calculating the theoretical global conductance

$$C_{\text{th}} = \frac{Q'}{Q'_{\max}} \tag{17}$$

where $Q'_{\max}$ is the constant ceiling value provided by Eq. (9). The ideal design is the isothermal wall, for which $C_{\text{th}} = 1$. In the opposite extreme, when $D_0$ is not small and $x_0$ approaches $L$, $C_{\text{th}}$ approaches $1 - 0.318 = 0.682$, which corresponds to a $L$-long wall with uniform heat flux and $T_{\max}$ at $x = L$. Eq. (16) summarizes the maximal performance of all the designs contained between the two limits. The performance of all the designs that have not been optimized is characterized by $C_{\text{th}}$ values smaller than those given by Eqs. (16) and (17).

## 4. Numerical formulation

In the second part of this study we simulated numerically the flow and heat transfer in the vicinity of the wall with discrete heat sources, Fig. 2. The wall of length $L$ is the bottom side of a channel of spacing $D$. The upper side is modeled as adiabatic. Cold fluid is pushed into the channel by a flow that approaches with a free-stream velocity $U_\infty$. The mass, momentum and energy equations were simplified in accordance with the assumption of two dimensional steady state laminar flow with constant properties,

$$\frac{\partial u}{\partial x} + \frac{\partial v}{\partial y} = 0 \tag{18}$$

$$\rho\left(u\frac{\partial u}{\partial x} + v\frac{\partial u}{\partial y}\right) = -\frac{\partial P}{\partial x} + \mu\nabla^2 u \tag{19}$$

$$\rho\left(u\frac{\partial v}{\partial x} + v\frac{\partial v}{\partial y}\right) = -\frac{\partial P}{\partial y} + \mu\nabla^2 v \tag{20}$$

$$\rho c_P\left(u\frac{\partial T}{\partial x} + v\frac{\partial T}{\partial y}\right) = k\nabla^2 T \tag{21}$$

where $\nabla^2 = \partial^2/\partial x^2 + \partial^2/\partial y^2$. The variables and properties are defined in the Nomenclature. The numerical domain is composed of the channel ($L \times D$), an upstream section ($L_u \times D$) and a downstream section ($L_d \times D$): see Fig. 2. These extensions of the numerical domain are important and possibly critical in channels with small aspect ratios, $L/D < 10$, even at high flow velocities, which is the domain studied in the present work. From a practical point of view, these extensions were introduced to mimic a free stream condition, which describes a more realistic situation than the discretization of the fluid between the parallel plates only ($L \times D$). From the numerical point of view, the upstream reservoir frees the flow to develop itself hydraulically starting at the entrance plane of the channel, while the inlet uniform flow boundary condition is specified at the entrance plane of the upstream reservoir. By doing this, no velocities profiles are assumed at the channel entrance. The downstream reservoir also delayed the imposition of an unrealistic outlet boundary condition on the exit plane of the channel. Accuracy tests showed if $L_u = L_d = 0.5\,L$, the total heat transfer rate is insensible (with changes less than 1%) to any further doubling of $L_u$ and $L_d$.

The nondimensionalization of Eqs. (18)–(21) is based on the free-stream velocity $U_\infty$, which is fixed: the

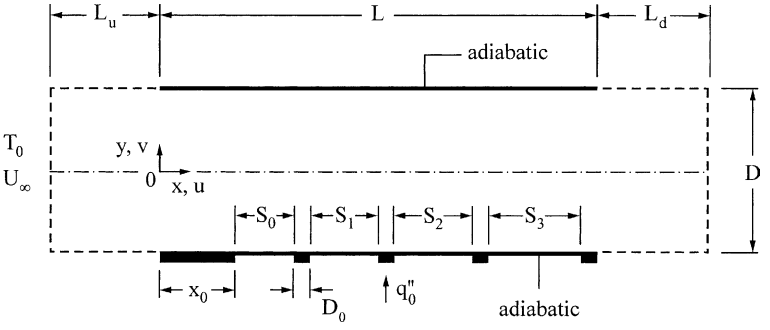


Fig. 2. Two-dimensional channel with discrete heat sources on one wall.

variables and properties are defined in the Nomenclature. The dimensionless variables are:

$$\left(\tilde{x},\tilde{y},\widetilde{D}_0,\widetilde{S}_i\right)=\frac{(x,y,D_0,S_i)}{L}\quad(\tilde{u},\tilde{v})=\frac{(u,v)}{U_\infty} \tag{22}$$

$$\widetilde{T}=\frac{T-T_\infty}{q_0''L/k}\quad \widetilde{P}=\frac{P}{\rho U_\infty^2} \tag{23}$$

Eqs. (18)–(21) become

$$\frac{\partial\tilde{u}}{\partial\tilde{x}}+\frac{\partial\tilde{v}}{\partial\tilde{y}}=0 \tag{24}$$

$$\left(\tilde{u}\frac{\partial\tilde{u}}{\partial\tilde{x}}+\tilde{v}\frac{\partial\tilde{u}}{\partial\tilde{y}}\right)=-\frac{\partial\widetilde{P}}{\partial\tilde{x}}+\frac{1}{Re}\nabla^2\tilde{u} \tag{25}$$

$$\left(\tilde{u}\frac{\partial\tilde{v}}{\partial\tilde{x}}+\tilde{v}\frac{\partial\tilde{v}}{\partial\tilde{y}}\right)=-\frac{\partial\widetilde{P}}{\partial\tilde{y}}+\frac{1}{Re}\nabla^2\tilde{v} \tag{26}$$

$$\left(\tilde{u}\frac{\partial\widetilde{T}}{\partial\tilde{x}}+\tilde{v}\frac{\partial\widetilde{T}}{\partial\tilde{y}}\right)=\frac{1}{RePr}\nabla^2\widetilde{T} \tag{27}$$

where

$$Re=\frac{U_\infty L}{\nu}\text{ and }Pr=\frac{\nu}{\alpha} \tag{28}$$

The boundary conditions are: $\tilde{u}=1$ and $\widetilde{T}_0=0$ at the inlet of the computational domain; $\partial\tilde{u}/\partial\tilde{x}=\partial\tilde{v}/\partial\tilde{x}=\partial\widetilde{T}/\partial\tilde{x}=0$ at the outlet, free slip and no penetration at the fluid-fluid interface (symmetry); no-slip and no penetration at the solid surfaces. The thermal boundary conditions on the discretely heated wall are uniform heat flux over each heat source ($\tilde{q}=1$), and adiabatic over the wall sections located between heat sources. The uniform heat flux condition on the heat source surface is

$$\frac{\partial T}{\partial y}=-\frac{q_0''}{k}\text{ at }y=-D/2 \tag{29}$$

The optimization process consisted of simulating and comparing a large number of wall heating configurations. Eqs. (24)–(27) were solved using a finite element code [13]. The computational cost was fairly small, taking no more than 90 s per simulation, on a Sun Blade 1000 (Ultra Spark III) Unix machine. The numerical domain was discretized using quadrilateral elements with 9 nodes per element. A penalty function was applied to eliminate the explicit appearance of the pressure term in Eqs. (25) and (26). The penalty parameter was set equal $10^{-8}$. The Newton–Raphson method was used to solve the nonlinear system of Eqs. (24)–(27). The convergence criteria adopted for the velocity and residual vectors were:

$$\frac{\left\|u^{(n)}-u^{(n-1)}\right\|}{\left\|u^{(n)}\right\|}\leqslant 0.001,\quad \frac{\left\|R(u^{(n)})\right\|}{\|R_0\|}\leqslant 0.001 \tag{30}$$

where $u$ is the velocity vector solution, and $R$ is the residual vector.

The numerical work started with a detailed grid generation. Because boundary layers are present, a nonuniform grid was used in the $y$ direction, and the smallest elements were placed close to the walls. Mesh independence was achieved when less than 101 nodes per unit of dimensionless length were used in both directions, although for simplicity, we decided to use 101 nodes per unit of dimensionless length in both directions. Grid tests were performed by monitoring the applied heat flux

$$\tilde{q}=\frac{q}{q_0''} \tag{31}$$

and the maximal temperature reached at a point on the bottom wall,

$$\widetilde{T}_{\max}=\frac{T_{\max}-T_\infty}{q_0''L/k} \tag{32}$$

Two different configurations were selected to show how the grid independence was achieved: one with a small heat source of length $\widetilde{D}_0=0.1$, and another with uniform heat flux applied over the entire bottom wall $\widetilde{D}_0=1$. Table 1 shows that $\tilde{q}$ and $\widetilde{T}_{\max}$ are insensitive to any further grid refinement when the grid has 51 nodes per $L$. The importance of monitoring the calculated dimensionless heat flux $\tilde{q}$ stems from the fact that in this way we can check the code and the nondimensionalization. For example, if the code returns the calculated $\tilde{q}$ equal or at least very close to the applied one, it means

Table 1
Grid refinement test ($\widetilde{D}_0=0.1$, $\widetilde{S}_0=0$, $\widetilde{D}=0.3$, $Re=100$ and $Pr=0.7$)

| Nodes per $L$ | Nodes | Elements | $\tilde{q}$ | $\left\|\frac{\tilde{q}^i-\tilde{q}^{i+1}}{\tilde{q}^{i+1}}\right\|$ | $\widetilde{T}_{\max}$ | $\left\|\frac{\widetilde{T}^i_{\max}-\widetilde{T}^{i+1}_{\max}}{T^{i+1}_{\max}}\right\|$ |
|---|---|---|---|---|---|---|
| 25 | 357 | 131 | 0.8703 | – | 0.04566 | – |
| 51 | 1515 | 464 | 0.9506 | 0.0844 | 0.04777 | 0.0441 |
| 75 | 3473 | 997 | 0.9664 | 0.0163 | 0.04847 | 0.0144 |
| 101 | 6231 | 1730 | 0.9736 | 0.0073 | 0.04867 | 0.0041 |
| 201 | 24461 | 6460 | 0.9860 | 0.0050 | 0.04885 | 0.0037 |

Table 2
Grid refinement test ($\widetilde{D}_0 = 1$, $\widetilde{D} = 0.3$ and $Pr = 0.7$)

| Nodes per $L$ | Nodes | Elements | $\widetilde{T}_{max}$ | | | |
|---|---|---|---|---|---|---|
| | | | $Re = 10^2$ | $10^3$ | $10^4$ | $10^5$ |
| 25 | 35 | 131 | 0.14561 | 0.05944 | 0.02381 | – |
| 51 | 1515 | 464 | 0.14655 | 0.06048 | 0.02183 | 0.00802 |
| 75 | 3473 | 997 | 0.14674 | 0.06079 | 0.02205 | 0.00763 |
| 101 | 6231 | 1730 | 0.14681 | 0.06081 | 0.02200 | 0.00740 |
| 201 | 24461 | 6460 | 0.14692 | 0.06092 | 0.02204 | 0.00739 |

that the code is correct, and that we may proceed to another level of correcting and improving the numerical scheme. Table 2 shows that $\widetilde{T}_{max}$ is also insensitive to further grinding with less than 101 nodes per $L$ when one large heat source is placed on the bottom wall.

The spacing $D$ between the walls of the channel has a strong effect on the global conductance between the walls and the fluid [14]. The optimal spacing for maximal heat transfer rate density has been correlated by

$$\widetilde{D}_{opt} \cong 3.2\left(\frac{b}{L}\right)^{1/2} Re^{-1/2} Pr^{-1/4} \tag{33}$$

where $b$ is the total length occupied by the heated section, i.e., the flush-mounted sources plus the unheated patches between them. The optimal spacing is such that the boundary layers merge at the channel exit. Based on Eq. (33), we can determine the appropriate $D$ spacing that leads the numerical domain towards a similar configuration described previously in Sections 2 and 3. In other words, the numerical $\widetilde{D}$ spacing was selected to be greater than $\widetilde{D}_{opt}$, for example $\widetilde{D} = 0.3$ in Figs. 3 and 4. This means that in all the numerical simulations the boundary layers are distinct.

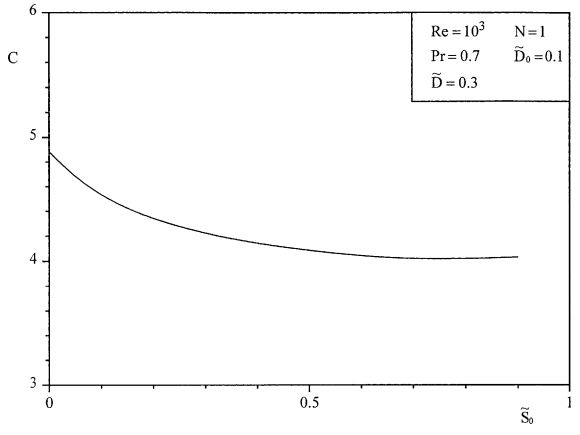


Fig. 3. The maximization of the global conductance when only one heat source is present.

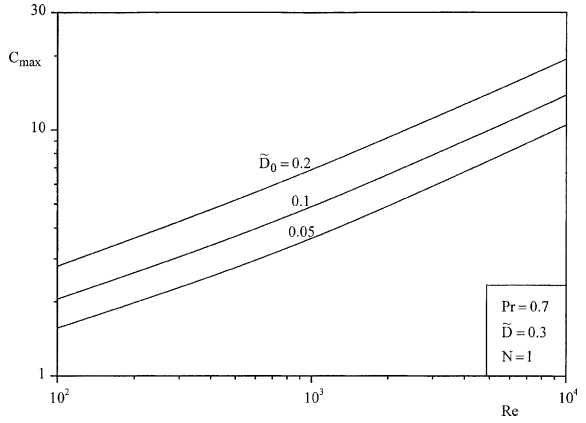


Fig. 4. The maximized global conductance that corresponds to the optimized location of the single heat source.

## 5. Optimal distribution of heat sources

The global conductance of the forced convection configuration is

$$C = \frac{Q'}{k(T_{max} - T_\infty)} \tag{34}$$

where $Q'$ is the total heat flow through the heat sources and $T_{max}$ is the maximal temperature that may occur at any point on the plate. The dimensionless conductance expresses the relation between a fixed heat input and the largest temperature difference between the solid wall and the coolant. The maximization of $C$ is equivalent to the minimization of $T_{max}$.

Fig. 3 shows the effect of $\widetilde{S}_0$ on $C$ when only one heat source is attached to the plate. The location of the heat source has a strong effect on the global conductance: $C$ increases by 25% if the heat source is moved from near the outlet ($\widetilde{S}_0 = 0.9$) to the inlet ($\widetilde{S}_0 = 0$). The same trend was found in all the cases simulated numerically in the range $10^2 \leqslant Re \leqslant 10^4$ and $0.05 \leqslant \widetilde{D}_0 \leqslant 0.2$.

Fig. 4 reports the maximized global conductance that corresponds to the optimized single-source locations, $\widetilde{S}_{0,opt} = 0$ (e.g. Fig. 3). On this log–log graph, $C_{max}$ is proportional to $Re^{0.47}$ when $Re \cong 10^4$. Note also the

constancy of the ratio between the $C_{max}$ values of successive curves, where $\widetilde{D}_0$ changes by a factor of 1/2,

$$\frac{C_{max}(\widetilde{D}_0 = 0.05)}{C_{max}(\widetilde{D}_0 = 0.1)} \cong 0.42 \quad \frac{C_{max}(\widetilde{D}_0 = 0.1)}{C_{max}(\widetilde{D}_0 = 0.2)} \cong 0.35 \qquad (35)$$

Complexity of geometry and computation increases as two heat sources of equal strength ($\widetilde{D}_0$) are placed on the bottom wall of the flow channel. There are two degrees of freedom, the longitudinal spacings $\widetilde{S}_0$ and $\widetilde{S}_1$. The optimal configuration was found by performing two nested loops. In the inner loop $\widetilde{S}_0$ was fixed, and $\widetilde{S}_1$ varied until $C$ reached $C_{max}$. In the outer loop the function $C_{max}$ ($\widetilde{S}_0$) was maximized by repeating the inner loop for several close values of $\widetilde{S}_0$. The maximal value of $C_{max}$ is labeled $C_{2m}$, and occurs when $\widetilde{S}_0$ and $\widetilde{S}_1$ reach their optimal values.

Throughout the $Re$ and $\widetilde{D}_0$ range investigated numerically, we found that $\widetilde{S}_{0,opt} = 0$, i.e. the best position for the first heat source is at the start of the boundary layer. This conclusion is consistent with what we found in Section 3 and Fig. 3.

The second heat source has an optimal position downstream, which is reported in Fig. 5. The second heat source migrates toward the start of the boundary layer as $Re$ increases. This trend is in agreement with the analytical results developed in Sections 2 and 3. Furthermore, Fig. 5 reveals a 'transition' at $Re \sim 10^3$. When $Re \lesssim 10^3$, the best location for the second heat source is far from the entrance, and is insensitive to changes in $Re$. It is downstream, far from the entrance, that the second heat source can release its heat flux without excessively high temperatures on the wall. When $Re > 10^3$, the fast flow prevents the occurrence of hot spots in the downstream section, and $\widetilde{S}_{1,opt}$ migrates safely toward the tip of the boundary layer. Fig. 5 suggests that when $Re$ reaches above $10^4$ the second heat source comes to reside flush against the first heat source. This behavior was anticipated analytically in Section 3.

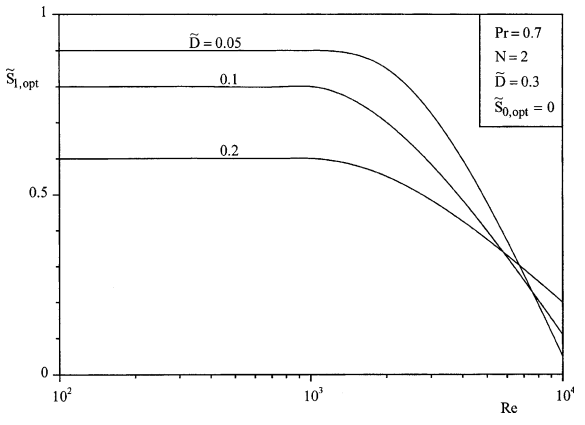


Fig. 5. The optimal locations of two heat sources.

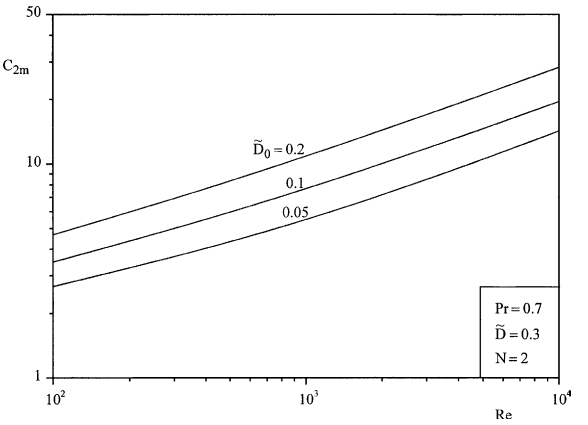


Fig. 6. The maximized global conductance that corresponds to the optimized placement of two heat sources.

Fig. 6 summarizes the results for the twice-maximized global conductance ($C_{2m}$) that corresponds to $\widetilde{S}_{0,opt} = 0$ and the $\widetilde{S}_{1,opt}$ values shown in Fig. 5. Noteworthy are the similarities between Figs. 6 and 4, because $C_{2m}$ is also proportional to $Re^{0.47}$.

Another interesting feature emerges when the total heated area fraction of the wall is fixed. For example, when the heated area fraction is fixed at $N\widetilde{D}_0 = 0.1$, and if $Re = 10^2$, then for one heat source ($N = 1$) Fig. 4 shows that $C = 2.054$, while for $N = 2$ Fig. 6 reports $C = 2.673$. The change from one optimally placed heat source (Fig. 4) to two optimally placed sources (Fig. 6) results in a 30% improvement in global performance. This stepwise improvement depends on Reynolds number.

If $Re$ is set equal to $10^3$ and $10^4$, then the relative improvement becomes 7% and, respectively 3%. Diminishing returns are reached at higher Reynolds numbers because faster flows 'shave' the temperature peaks (hot spots) more effectively. The same relative increases in global conductance $C$ are registered if the total heated area fraction $N\widetilde{D}_0$ is fixed at 0.2 in the range $10^2 \leqslant Re \leqslant 10^4$. The main conclusion is that the global performance increases as the optimized complexity of the heating arrangement increases. This is in agreement with the analysis of Sections 1 and 2.

The method illustrated until now for one and two heat sources can be applied to the optimization of more complex arrangements. Next on the path toward greater complexity is the wall with three heat sources. There are three degrees of freedom ($\widetilde{S}_0, \widetilde{S}_1, \widetilde{S}_2$), and three nested optimization loops. The optimal position for the first heat source is once again at the start of the boundary layer, $\widetilde{S}_{0,opt} = 0$. The optimized second and third spacings are reported in Fig. 7. The second heat source migrates toward the first as $Re$ increases, and rests flush against it when $Re \gtrsim 10^3$. The third heat source is always located at the trailing edge of the wall, in spite of what

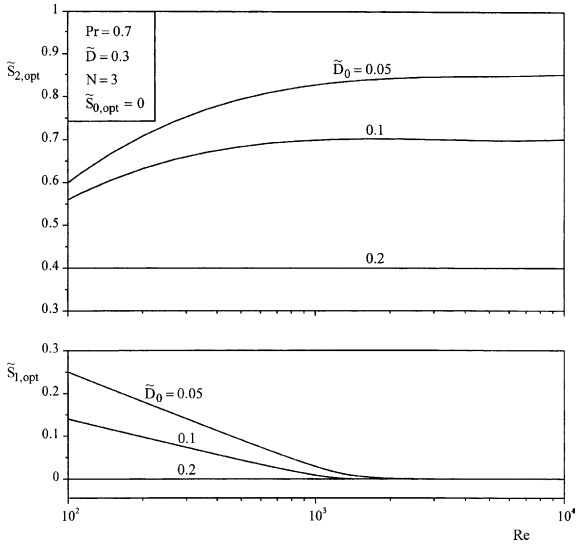


Fig. 7. The optimal locations of three heat sources.

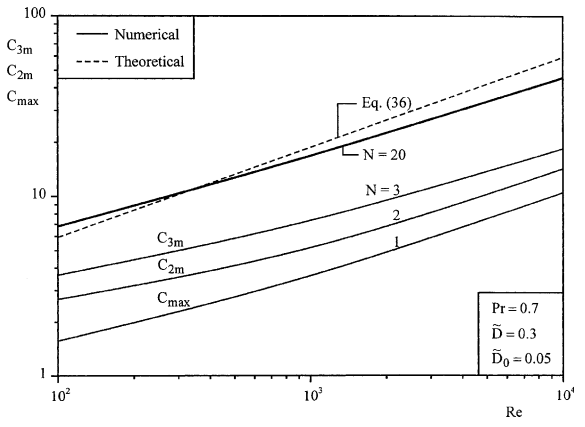


Fig. 8. The effect of the number of discrete heat sources on the maximized global conductance when $\widetilde{D}_0 = 0.5$.

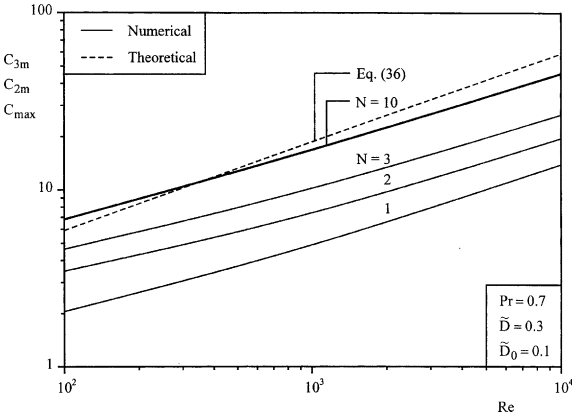


Fig. 9. The effect of the number of discrete heat sources on the maximized global conductance when $\widetilde{D}_0 = 0.1$.

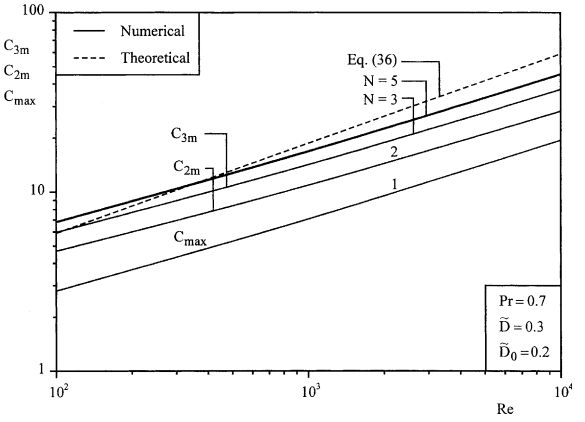


Fig. 10. The effect of the number of discrete heat sources on the maximized global conductance when $\widetilde{D}_0 = 0.2$.

the upper frame of Fig. 7 might suggest as $\widetilde{S}_{2,\mathrm{opt}}$ increases with $Re$. This can be verified by adding up the lengths occupied by the three heat sources and their spacings, $3\widetilde{D}_0 + \widetilde{S}_{1,\mathrm{opt}} + \widetilde{S}_{2,\mathrm{opt}} = 1$.

The maximized global conductance for the wall with three heat sources ($C_{3\mathrm{m}}$) is reported in Figs. 8–10. Each graph is made for a single heat source length ($\widetilde{D}_0$), and on it we compare $C_{3\mathrm{m}}$ with the corresponding values obtained for $C_{2\mathrm{m}}$ and $C_{\max}$. In other words, each of Figs. 8–10 illustrates the effect of optimized complexity ($N$) on the maximized global performance of the multi-scale arrangement.

The chief conclusion is that performance increases as complexity increases. In all the cases documented in this study the performance gains in global conductance are significant for each step increase in $N$. Viewed together, Figs. 8–10 also show the effect of the heat source size ($\widetilde{D}_0$), which represents the 'coarseness' of the heat flow structure. Diminishing returns are visible in Fig. 10, where $\widetilde{D}_0$ has the largest value: the jump from $N = 2$ to $N = 3$ (or from $C_{2\mathrm{m}}$ to $C_{3\mathrm{m}}$) is smaller than from $N = 1$ to $N = 2$ (or from $C_{\max}$ to $C_{2\mathrm{m}}$).

The bold and dashed curves in Fig. 8 are the same as the top curves in Figs. 9 and 10. The bold curve represents the performance of the wall with the largest number of heat sources, $N_{\max} = 1/\widetilde{D}_0$, all mounted flush against each other. In this limit no optimization is possible: all the spacings are zero, however, $N$ depends on $\widetilde{D}_0$. The dashed curves represent the maximal global conductance determined theoretically, which is obtained by rearranging Eq. (9) as

$$C = \frac{Q'_{\max}}{k(T_{\max} - T_\infty)} = 0.664 Pr^{1/3} Re^{1/2} \tag{36}$$

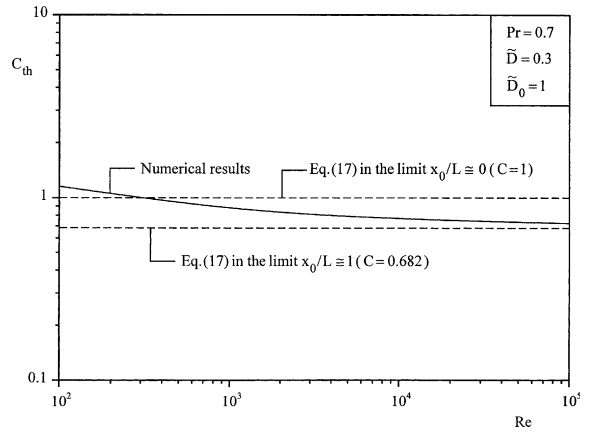


Fig. 11. Maximal global conductance versus the Reynolds number: comparison between the theoretical solution and the numerical results.

These ceiling curves are useful in several respects. First, the diminishing returns noted in the preceding paragraph are pronounced when the maximized conductances ($C_{max}$, $C_{2m}$, $C_{3m}$) are close to the ceiling conductance. This happens when the heat source size is large, and when the number of heat sources that could be installed is small.

Another thought that comes from plotting the bold curves in Figs. 8–10 is whether the wall with continuous and uniform heat flux is the best design. We know from Sections 2 and 3 that this is not the case, however, Figs. 8–10 seem to suggest it. In order to verify this, Eq. (17) was nondimensionalized and applied to a configuration where the entire bottom wall of the channel is subjected to a uniform heat dimensionless heat flux $\tilde{q} = 1$. In this case

$$C_{th} = \frac{1}{\widetilde{T}_{max} 0.664 Pr^{1/3} Re^{1/2}} \tag{37}$$

where $\widetilde{T}_{max}$ is the maximum dimensionless temperature obtained numerically. Fig. 11 shows that the $C_{th}$ values of Eq. (37) converge asymptotically to the theoretical constant $\cong 0.682$ as the Reynolds number increases, presenting then a good agreement between the theoretical derivation obtained in Section 3 and the numerical results. This means that the bold ceiling curves presented in Figs. 8–10 do not represent the best design, which in fact belongs to a much more complex design (i.e., ideal configuration). According to Eq. (17), the gap between the ideal configuration ($C_{th} = 1$) and the numerical results for $\widetilde{D}_0 = 1$ ($C_{th} \cong 0.682$) will be filled by a complex distribution of heat sources each one with a length of $D_0/L \to 0$. The higher the complexity, the better the thermal performance. Furthermore, it also should be noticed that the theory breaks down at low Reynolds numbers, $Re \leqslant 200$.

## 6. Conclusions

This paper addressed the fundamental problem of how to allocate discrete heat sources to the space on a wall cooled by forced convection. The objective was to maximize the global conductance between the wall and the coolant. The analysis showed that the heat sources must be distributed nonuniformly on the wall, and that the optimal spacings between heat sources depend on the Reynolds number. This work dealt specifically with forced convection, however, the same constructal principle can be used to determine optimal spatial allocation in natural convection [15].

Two distinct regions were identified on a wall with optimally distributed heat sources. The first region is located upstream of a transition point, $x_0$, near the tip of the boundary layer. In this region the heat sources should be mounted flush against each other. The second region is located downstream of $x_0$, and is characterized by a nonuniform distribution of heat sources, with the smallest spacings between the heat sources close to $x_0$, and the largest near the trailing edge.

The results of analytical optimization were verified numerically. The flow in a discretely heated channel was simulated numerically. The global conductance was maximized for configurations with one, two and three heat sources ($C_{max}$, $C_{2m}$ and $C_{3m}$), and in all cases the wall was covered incompletely by heat sources, $N D_0 < L$. The numerical results showed that the migration of the heat sources towards the tip of the boundary layer depends strongly on the Reynolds number and the heat source length $D_0$. Diminishing returns were also observed: the stepwise increase in global conductance decreases as the number of heat sources increases. The maximized global conductance was found to be approximately proportional to $Re^{0.47}$, regardless of $N$ or $D_0$. The results also showed that for fixed a heated area, the global conductance increases with the number of optimally placed heat sources.

Finally, in Fig. 11 we showed that the best possible design is not the one in which the wall is heated uniformly ($N\ D_0 = L$). The best are the highly complex configuration characterized by large numbers of optimally placed heat sources. This occurs in the limit of $x_0/L \to 0$. This direction could be explored numerically in future work, filling the gap between numerical results presented in this paper and the ideal configurations identified in Sections 2 and 3.

## Acknowledgements

A.K. da Silva thanks the Brazilian National Research Council (CNPq-Conselho Nacional de Desenvolvimento Científico e Tecnológico) for the award of a

scholarship no 200021/01-1. A. Bejan's work was supported by the National Science Foundation.

## References

[1] A. Bejan, Shape and Structure, from Engineering to Nature, Cambridge University Press, Cambridge, UK, 2000.
[2] F.P. Incropera, J.S. Kerby, D.F. Moffatt, S. Ramadhyani, Convection heat transfer from discrete heat sources in a rectangular channel, Int. J. Heat Mass Transfer 29 (1986) 1051–1058.
[3] A.B. McEntire, B.W. Webb, Local forced convective heat transfer from protruding and flush-mounted two-dimensional discrete heat sources, Int. J. Heat Mass Transfer 33 (1990) 1521–1533.
[4] H.V. Mahaney, F.P. Incropera, S. Ramadhyani, Comparison of predicted and measured mixed convection heat transfer from an array of discrete sources in a horizontal rectangular channel, Int. J. Heat Mass Transfer 33 (1990) 1233–1245.
[5] H.J. Shaw, W.L. Chen, Laminar forced-convection in a channel with arrays of thermal sources, Warme Stoffubertrag 26 (1991) 195–201.
[6] C.Y. Wang, Optimum placement of heat-sources in forced-convection, J. Heat Transfer 114 (1992) 508–510.
[7] A. Gupta, Y. Jaluria, Forced convective liquid cooling of arrays of protruding heated elements mounted in a rectangular duct, J. Electron. Packaging 120 (1998) 243–252.
[8] C.P. Tso, G.P. Xu, K.W. Tou, An experimental study on forced convection heat transfer from flush-mounted discrete heat sources, J. Heat Transfer 121 (1999) 326–332.
[9] M.M. Rahman, J. Raghavan, Transient response of protruding electronic modules exposed to horizontal cross flow, Int. J. Heat Fluid Flow 20 (1999) 48–59.
[10] G.I. Sultan, Enhancing forced convection heat transfer from multiple protruding heat sources simulating electronics components in a horizontal channel by passive cooling, Microelectron. J. 31 (2000) 773–779.
[11] S. Chen, Y. Liu, S.F. Chan, C.W. Leung, T.L. Chan, Experimental study of optimum spacing problem in the cooling of simulated electronics package, Heat Mass Transfer 37 (2001) 251–257.
[12] A. Bejan, Convection Heat Transfer, second ed., Wiley, New York, 1995.
[13] Fluid Dynamics International, FIDAP Theory Manual, Evanston, IL,1998.
[14] A.M. Morega, A. Bejan, Optimal spacing of parallel boards with discrete heat sources cooled by laminar forced convection, Num. Heat Transfer—A 25 (1994) 373–392.
[15] A.K. da Silva, S. Lorente, A. Bejan, Optimal distribution of discrete heat sources on a wall with natural convection, Int. J. Heat Mass Transfer 47 (2004) 203–214.